Fragile Insulator and Electronic Nematicity in a Graphene Moiré System

Lei Chen†, Haoyu Hu†, Qimiao Si*

Department of Physics and Astronomy & Rice Center for Quantum Materials, Rice University, Houston, Texas 77005, USA

Strongly correlated quantum matter exhibits a rich variety of remarkable properties, but the organizing principles that underlie the behavior remain to be established. Graphene heterostructures, which can host narrow moiré electron bands[1] that amplify the correlation effect, represent a new setting to make progress on this overarching issue. In such correlated moiré systems, an insulating state is a prominent feature of the phase diagram and may hold the key to understanding the basic physics. Here we advance the notion of a fragile insulator, a correlation-driven insulating state that is on the verge of a delocalization transition into a bad metal. Using a realistic multiorbital Hubbard model as a prototype for narrow band moiré systems, we realize such a fragile insulator and demonstrate a nematic order in this state as well as in the nearby bad metal regime. Our results are consistent with the observed electronic anisotropy in the graphene moiré systems[2–5] and provide a natural understanding of what happens when the insulator is tuned into a bad metal[6–8]. We propose the fragile insulator and the accompanying bad metal as competing states at integer fillings that analogously anchor the overall phase diagram of the correlated moiré systems and beyond.

E-mail: *qmsi@rice.edu

†L. C. and H. H. contributed equally to this work.

Strongly correlated systems are epitomized by cuprate superconductors, where a robust insulating state serves as the "parent" from which high temperature superconductivity develops upon introducing charge carriers[9]. Correlated insulators and superconductivity also emerge in the twisted bilayer graphene (TBG) at magic angles[10–13], trilayer graphene heterostructures with hexagonal boron nitride substrate (TLG/hBN)[14,15] and related structures. The narrowness of the moiré bands at the magic angles[1] implies that the relative strength of the electron correlations is enhanced, which has been demonstrated by spectroscopic means[2–4,16]. The insulators appear at the partial but integer fillings of the moiré bands, where the system would have been metallic in the absence of electron correlations, while superconductivity arises when the charge carrier concentration is tuned away from such fillings. By analogy with the cuprates, the insulating phase is believed to be key to elucidating the correlation physics of the moiré systems[17–22]. However, understanding the insulators remains a pressing open question.

Here, we address this issue, departing from several motivating factors. One consideration concerns the insulating nature *per se*. The insulating behavior develops at energy scales that can be low compared to either the effective Coulomb repulsion (U) or the width (W) of the moiré bands. For instance, for the magic-angle TBG devices at half filling ($\nu = 2$, corresponding to 1 electron or hole per valley per moiré unit cell), the electrical resistivity shows an insulating-like temperature dependence below about 4 K (Refs. 10,11,18), which is more than one decade lower than the scale $U \sim W \sim 10$ meV. Moreover, recent experiments have shown that the insulator can be tuned away quantum mechanically: This happens upon varying the strength of the electron correlations without changing the carrier concentration, while superconductivity persists; the result raises the question of whether the insulator anchors the phase diagram at all[6–8].

Another consideration is about electronic orders, a rich landscape of which is one of the salient characteristics of strongly correlated electron systems[9,23,24]. Recently, measurements by scanning tunneling microscopy (STM)[2–4] have revealed evidence for electronic nematic correlation in the normal state (above the superconducting transition temperature) of the magic-angle TBG. The local density of states shows a three-fold anisotropy[2], implying a large nematic susceptibility and possibly even a nematic order. Importantly, the effect maximizes near the insulating phase of the half-filled moiré bands (*i.e.*, two electrons or holes per unit cell of the moiré superlattice)[2]. These STM observations are complemented by transport measurements[5], which furthermore connect the nematicity with superconductivity. Understanding the nematic correlation is important, as it is primed for clues about the underlying correlation physics.

The system we choose to focus on as a prototype case is TLG/hBN, where the correlation physics can be isolated and non-perturbative theoretical analyses are possible. In this system, the moiré superstructure (Fig. 1a) results from a small difference between the in-plane lattice constants of the ABC stacked TLG (see Supplementary Information, Fig. S1) and hBN[14,15,25,26]. In the case of the magic-angle TBG, a topological obstruction to the construction of Wannier orbitals for their moiré bands has been actively discussed (for example, Refs. 27,28). The TLG/hBN structure under a particular direction of the perpendicular voltage bias, while having electronic properties with considerable similarities to those of the magic-angle TBG, do not face such an obstruction[14,15]. Consequently, their moiré bands are faithfully represented by a two-orbital Hubbard Hamiltonian[26], comprising the kinetic part, H_0, and the interaction part $H_U + H_V$ (see Methods). The reggime of prime interest corresponds to intermediate correlation, with the normalized interaction $U/W \sim O(1)$, which is difficult to access by perturbative expansions either in U/W or its inverse. Here, we investigate this regime using non-perturbative methods. Our primary tool will be the recently developed Variational Monte Carlo (VMC) method that incorporates the correlation effects of not only the Hubbard interaction but also the Hund's coupling[29] (see Methods).

We consider the half-filled case, keeping in mind the aforementioned motivations. To be definite, we focus on the case with a perpendicular voltage bias, which fixes the tight-binding parameters (see Fig. 1b, Methods and Supplementary Information) for H_0, and allows for an estimate of the parameters for both H_U (the onsite Hubbard interaction U and Hund's coupling J_H) and H_V (the density-density interaction V and spin-valley exchange interaction V_H between nearest-neighbor sites)[26]. A metal-insulator transition (MIT) could arise in the multiorbital model, in spite of having an even number of electrons per unit cell, due to the onsite interactions. We address their effects by performing a saddle-point analysis within a U(1) slave-spin method[30] (see Methods). Focusing on the paramagnetic phase that preserves the time reversal and translation symmetries, the quasiparticle weight is the same for the two valleys, $Z_+ = Z_- = Z$. The results of Z *vs.* U/W, for various values of the ratio J_H/U, are shown in Fig. 1c. In the absence of the Hund's coupling, $J_H = 0$, a metal-to-insulator transition occurs at $U_c(J_H = 0)/W \approx 1.65$. As Fig. 1c also shows, even a relatively small Hund's coupling considerably enhances the localization effect, and turns the threshold for the metal-insulator transition to about $U_c/W \approx 1$.

The metallic regime in proximity of the metal-to-insulator transition corresponds to a bad metal, where the quasiparticle weight Z is much reduced from the free-electron value 1 (Refs. 23,31). This motivates us to dub the insulating regime in proximity of the insulator-to-metal transition a

fragile insulator. In this regime, the insulating gap is considerably smaller than either U and W. Correspondingly, the temperature scale for the onset of the insulating behavior is expected to be small compared to U/k_B and W/k_B. We expect such behavior to occur in other integer fillings between charge neutrality and fully filled moiré bands, *albeit* with a different threshold interaction for the transition. For instance, a similar transition from bad metal to fragile insulator occurs at quarter filling ($\nu = 1$), as is also shown in Fig. 1c.

We next analyse the possible electronic orders. The effect of onsite interactions is studied using the VMC method that is non-perturbative in both the Hubbard interaction and Hund's coupling[29] (see Methods). In the intermediate correlation regime, we find that the ground state has a collinear antiferromagnetic (CAFM) order (Fig. 2a), with the pitch wavevector located at $\mathbf{Q} = \mathbf{M} = (0, \frac{2\sqrt{3}}{3}\pi)$ of the moiré Brillouin zone (BZ) [or equivalently $(\pi, \frac{\sqrt{3}}{3}\pi)$ and $(-\pi, \frac{\sqrt{3}}{3}\pi)$)]. Fig. 2c shows its energy to be lower than that of not only the paramagnetic phase (*i.e.*, without any order) but also the competing uniaxial antiferrovalley (UAFV) order (Fig. 2b). The corresponding magnetic order parameter m^2 (see Methods) is shown as a function of J_H/U for a fixed U/W (Fig. 2d) and *vs.* U/W for a fixed J_H/U (Fig. 2e) as a function of J_H/U. The magnetic order exits both in the fragile insulating and bad metal regimes.

This sets the stage to examine the nematicity. The nematic order is classified in terms of the breaking of the C_6 symmetry, which is an approximate symmetry of the system and exists in the model Hamiltonian, or the C_3 symmetry, which survives the weak couplings that exist in the system beyond the model[14,15,25,26]. The irreducible representations of the crystal point groups D_6 and D_3 are given in Table I. We find the relevant nematic order parameter σ to be in the E_2/E representation, respectively in the D_6/D_3 classification scheme (see Methods). The calculated nematic order parameter is shown in Fig. 3a,b, respectively as a function of J_H/U and *vs.* U/W. As a key result of our work, the nematic order parameter is nonzero both in the fragile insulator and bad metal regimes and, moreover, it varies smoothly between the two regimes.

It is important to assess the stability of this ground state against the intersite interactions, which are significant due to the size of the moiré unit cell. Consider first the nearest-neighbor exchange coupling V_H. Our VMC calculation finds the CAFM and associated nematic order to be stable for a range of this coupling, up to $V_H^1/W \approx 0.011$ (Fig. 3c). Above V_H^1, a ferromagnetic order becomes the ground state. Consider next the effect of the nearest-neighbor Coulomb repulsion V. The CAFM and associated nematic order are stable against the paramagnetic phase for a range of this coupling, up to $V^1/W \approx 0.31$ (Fig. 3d). It is instructive to note that the VMC

approach is non-perturbative and, therefore, advantageous in the intermediate correlation regime [$U/W \sim O(1)$] of interest here. For comparison, a self-consistent Hartree-Fock calculation is also carried out. It qualitatively captures the transition from CAFM to FM with the increasing exchange interaction V_H (see Supplementary Information, Fig. S5a), but misses the density-density interaction V-induced instability of the CAFM phase towards the paramagnetic phase (Supplementary Information, Fig. S5b). This result reflects the underestimation of the correlation effect by the Hartree-Fock method, especially for the paramagnetic state. Nonetheless, the Hartree-Fock calculation suggests that a sufficiently large V makes a charge order viable. The ordering wavevector is $\mathbf{K}$ (Fig. S5b); it is a three-sublattice order and is not expected to be accompanied by a nematic order. Note that our purpose is to use the well-defined Hamiltonian as a means to access the qualitative features of the overall phase diagram. Still, the threshold values we have determined, V_H^1/W and V^1/W, are competitive against the order-of-magnitude estimates for these parameters (which, at $\Delta_V = -20$ meV, are about 0.007 and 0.37, respectively[26]), suggesting that either a nematic order or an enhanced nematic fluctuation is to be expect for TLG/hBN.

We next turn to the experimental consequences of our results. First, the proximity of the fragile insulator to the delocalization transition implies the development of an energy scale that is small compared to the bare energies U and W. The insulating behavior only appears below this scale; above it, the system cannot be distinguished from what happens in the bad-metal regime. This provides a natural understanding of the experimental observations that the insulating-like temperature dependence appears in the electrical resistivity only at low temperatures[10,11]. Second, our finding that the fragile insulator is nematic allows for a microscopic understanding of the nematic correlations that have been observed in the normal state of the graphene moiré systems[2–5]. This is especially so given that the electronic anisotropy has been experimentally demonstrated to be peaked near half filling[2]. Third, we have found the electronic nematic order to appear at half filling, not only when the system is a fragile insulator but also when it is a bad metal. This leads us to predict that devices where the insulating phase has turned metallic[6–8] will also be nematic. Our prediction can be tested by measuring the electronic anisotropy in such moiré devices, using STM, transport and other experimental means.

Our finding also points towards a new organizing principle for the overall phase diagram of the narrow band moiré systems, as illustrated in Fig. 4. Our calculations show that the electronic nematic order appears both in the fragile insulator and in the bad metal. This illustrates the insensitivity of the underlying correlation physics to whether the parent system happens to be placed

on either side of the Mott transition, suggesting that both the fragile insulator and bad metal can anchor the overall phase diagram. The emerging picture is that the system away from any integer filling can be considered as being controlled by the Mott transition, the electronic localization-delocalization transition at the integer filling that links the fragile insulating and bad metallic regimes. By extension, when the carrier concentration is tuned away from half filling, the physics in the two cases is expected to be similar.

This picture is important for understanding another puzzle that has been highlighted by very recent experiments. It follows from Fig. 4 that, when the correlation strength is tuned down and the fragile insulator yields to a bad metal, the system at half filling continues to anchor qualitatively similar electronic behavior in the overall phase diagram, including the emergence of superconductivity. This is precisely what have been observed by the recent experiments of Refs. 6–8. By extension, these experimental observations are fully compatible with the superconductivity being (primarily) driven by electron-electron interactions.

The overall picture, Fig. 4, also suggests that the physics of the integer-filled moiré systems adiabatically evolves when the normalized interaction U/W is further enhanced from the fragile insulator/bad metal regime, where it is of order unity, to the regime where U/W is even larger and the correlated insulator is no longer fragile. The latter is likely the case in the recently realized moiré systems based on the transition-metal dichalcogenides[32–34]. In that regime, a robust Mott insulator at the integer fillings is expected to anchor the correlated electron physics at carrier concentrations away from those fillings. Thus, the correlation physics in these systems will be adiabatically connected to those in the intermediate correlation regime, although their energy scales, such as the exchange interactions as measured by their kinetic energy, will be smaller.

We close with two additional observations. First, our calculation at zero temperature sets the stage for addressing how the electronic orders melt away with increasing temperature. Because the nematic order is a composite of the spin degrees of freedom, it can occur even when the antiferromagnetic order parameter is fluctuating[23]. The latter corresponds to a nematic order that is not accompanied by any magnetic order. It will be instructive to experimentally study the temperature dependences of both the nematic correlations and magnetic responses in the correlated moiré systems. Second, by isolating the correlation effect in a model system, our work sets the stage to address how the interplay between the intermediate to strong correlations and bandstructure topology influences the fragile insulator, bad metal and electronic nematicity. The interplay promises to create new phases in the overall phase diagram, but whether and how it will enrich the relationship

between the fragile insulator and bad metal on the one hand, and superconductivity on the other, is an exciting open question. Empirically, the continued emergence of new members in the family of correlated moiré systems allows for ascertaining the similarities and differences between these members with differing bandstructure, which will surely illuminate this outstanding issue.

In summary, we have demonstrated an emergent fragile insulator in a graphene moiré system for the physically relevant intermediate correlation regime. This correlated insulator is accompanied by an electronic nematic order, which provides a natural understanding of the electronic anisotropy that has been observed in the magic-angle twisted bilayer graphene. Our work thus highlights the kind of clues that the electronic nematicity provides for the microscopic correlation physics, and motivates its search in related moiré systems. Finally, our work reveals that the same correlation physics is anchored by the parent system at an integer filling of the moiré lattice regardless of whether it is a fragile insulator or a bad metal. This finding explicates a striking puzzle on the phase diagram of the correlated moiré systems that has emerged from several very recent experiments. As such, our work uncovers a new organizing principle for the overall phase diagram of the correlated moiré systems, which also underscores the distinctive correlation parameter regime that these systems occupy compared to that for the cuprate superconductors. The new regime of parent system revealed here is sufficiently general that it may well control the physics of a variety of strongly correlated quantum structures and materials beyond the context of moiré systems.

---

1. Bistritzer, R. & MacDonald, A. H. Moiré bands in twisted double-layer graphene. *Proceedings of the National Academy of Sciences* **108**, 12233–12237 (2011).
2. Kerelsky, A. *et al.* Maximized electron interactions at the magic angle in twisted bilayer graphene. *Nature* **572**, 95–100 (2019).
3. Choi, Y. *et al.* Electronic correlations in twisted bilayer graphene near the magic angle. *Nature Physics* **15**, 1174–1180 (2019).
4. Jiang, Y. *et al.* Charge order and broken rotational symmetry in magic-angle twisted bilayer graphene. *Nature* **573**, 91–95 (2019).
5. Cao, Y. *et al.* Nematicity and competing orders in superconducting magic-angle graphene. *arXiv preprint arXiv:2004.04148* (2020).

6. Stepanov, P. *et al.* Untying the insulating and superconducting orders in magic-angle graphene. *Nature* **583**, 375–378 (2020).

7. Saito, Y., Ge, J., Watanabe, K., Taniguchi, T. & Young, A. F. Independent superconductors and correlated insulators in twisted bilayer graphene. *Nat. Phys.* (2020).

8. Arora, H. S. *et al.* Superconductivity in metallic twisted bilayer graphene stabilized by WSe2. *Nature* **583**, 379–384 (2020).

9. Lee, P. A., Nagaosa, N. & Wen, X.-G. Doping a mott insulator: Physics of high-temperature superconductivity. *Rev. Mod. Phys.* **78**, 17–85 (2006).

10. Cao, Y. *et al.* Magic-angle graphene superlattices: a new platform for unconventional superconductivity. *Nature* **556**, 43–50 (2018).

11. Cao, Y. *et al.* Correlated insulator behaviour at half-filling in magic-angle graphene superlattices. *Nature* **556**, 80–84 (2018).

12. Lu, X. *et al.* Superconductors, orbital magnets and correlated states in magic-angle bilayer graphene. *Nature* **574**, 653–657 (2019).

13. Yankowitz, M. *et al.* Tuning superconductivity in twisted bilayer graphene. *Science* **363**, 1059–1064 (2019).

14. Chen, G. *et al.* Evidence of a gate-tunable Mott insulator in a trilayer graphene moir superlattice. *Nature Physics* **15**, 237–241 (2019).

15. Chen, G. *et al.* Signatures of tunable superconductivity in a trilayer graphene moir superlattice. *Nature* **572**, 215–219 (2019).

16. Xie, Y. *et al.* Spectroscopic signatures of many-body correlations in magic-angle twisted bilayer graphene. *Nature* **572**, 101–105 (2019).

17. Xu, C. & Balents, L. Topological superconductivity in twisted multilayer graphene. *Phys. Rev. Lett.* **121**, 087001 (2018).

18. Dodaro, J. F., Kivelson, S. A., Schattner, Y., Sun, X. Q. & Wang, C. Phases of a phenomenological model of twisted bilayer graphene. *Phys. Rev. B* **98**, 075154 (2018).

19. Padhi, B., Setty, C. & Phillips, P. W. Doped twisted bilayer graphene near magic angles: Proximity to wigner crystallization, not mott insulation. *Nano letters* **18**, 6175–6180 (2018).

20. Thomson, A., Chatterjee, S., Sachdev, S. & Scheurer, M. S. Triangular antiferromagnetism on the honeycomb lattice of twisted bilayer graphene. *Phys. Rev. B* **98**, 075109 (2018).

21. Xie, M. & MacDonald, A. H. Nature of the correlated insulator states in twisted bilayer graphene.

Phys. Rev. Lett. **124**, 097601 (2020).

22. Pizarro, J., Calderón, M. & Bascones, E. The nature of correlations in the insulating states of twisted bilayer graphene. *Journal of Physics Communications* **3**, 035024 (2019).
23. Si, Q., Yu, R. & Abrahams, E. High-temperature superconductivity in iron pnictides and chalcogenides. *Nat. Rev. Mater.* **1**, 16017 (2016).
24. Keimer, B. & Moore, J. E. The physics of quantum materials. *Nat. Phys.* **13**, 1045 (2017).
25. Zhu, G.-Y., Xiang, T. & Zhang, G.-M. Inter-valley spiral order in the mott insulating state of a heterostructure of trilayer graphene-boron nitride. *Science Bulletin* **63**, 1087–1091 (2018).
26. Zhang, Y.-H. & Senthil, T. Bridging hubbard model physics and quantum hall physics in trilayer graphene/$h-\mathrm{BN}$ moiré superlattice. *Phys. Rev. B* **99**, 205150 (2019).
27. Po, H. C., Zou, L., Vishwanath, A. & Senthil, T. Origin of mott insulating behavior and superconductivity in twisted bilayer graphene. *Phys. Rev. X* **8**, 031089 (2018).
28. Yuan, N. F. Q. & Fu, L. Model for the metal-insulator transition in graphene superlattices and beyond. *Phys. Rev. B* **98**, 045103 (2018).
29. Hu, W.-J. *et al.* Nematic and antiferromagnetic quantum criticality in a multi-orbital hubbard model for iron pnictides. *arXiv preprint arXiv:1903.12625* (2019).
30. Yu, R. & Si, Q. U(1) slave-spin theory and its application to mott transition in a multiorbital model for iron pnictides. *Phys. Rev. B* **86**, 085104 (2012).
31. Hussey, N. E., Takenaka, K. & Takagi, H. Universality of the Mott–Ioffe–Regel limit in metals. *Philos. Mag.* **84**, 2847 (2004).
32. Tang, Y. *et al.* Simulation of Hubbard model physics in WSe 2 /WS 2 moir superlattices. *Nature* **579**, 353–358 (2020).
33. Regan, E. C. *et al.* Mott and generalized Wigner crystal states in WSe 2 /WS 2 moir superlattices. *Nature* **579**, 359–363 (2020).
34. Wang, L. *et al.* Correlated electronic phases in twisted bilayer transition metal dichalcogenides. *Nature Materials* 1–6 (2020).
35. Koshino, M. & McCann, E. Trigonal warping and berry's phase $n\pi$ in abc-stacked multilayer graphene. *Phys. Rev. B* **80**, 165409 (2009).
36. Zhang, F., Sahu, B., Min, H. & MacDonald, A. H. Band structure of abc-stacked graphene trilayers. *Phys. Rev. B* **82**, 035409 (2010).
37. Kumar, A. *et al.* Integer quantum hall effect in trilayer graphene. *Phys. Rev. Lett.* **107**, 126806 (2011).

38. Capello, M., Becca, F., Fabrizio, M., Sorella, S. & Tosatti, E. Variational description of mott insulators. *Phys. Rev. Lett.* **94**, 026406 (2005).

39. Zhang, Y.-H., Mao, D., Cao, Y., Jarillo-Herrero, P. & Senthil, T. Nearly flat chern bands in moiré superlattices. *Phys. Rev. B* **99**, 075127 (2019).

40. McCann, E. & Koshino, M. The electronic properties of bilayer graphene. *Reports on Progress in Physics* **76**, 056503 (2013).

41. Tocchio, L. F., Becca, F. & Sorella, S. Hidden mott transition and large-u superconductivity in the two-dimensional hubbard model. *Phys. Rev. B* **94**, 195126 (2016).

42. De Franco, C., Tocchio, L. F. & Becca, F. Metal-insulator transitions, superconductivity, and magnetism in the two-band hubbard model. *Phys. Rev. B* **98**, 075117 (2018).

Acknowledgments

We acknowledge useful discussions with D. P. Arovas, F. Becca, D. Goldhaber-Gordon, W.-J. Hu, A. H. MacDonald, A. Pasupathy, T. Senthil and J. Shan. This work has been supported in part by the U.S. DOE, BES under Award # DE-SC0018197 and the Robert A. Welch Foundation Grant No. C-1411. The majority of the computational calculations have been performed on the Shared University Grid at Rice funded by NSF under Grant EIA-0216467, a partnership between Rice University, Sun Microsystems, and Sigma Solutions, Inc., the Big-Data Private-Cloud Research Cyberinfrastructure MRI-award funded by NSF under Grant No. CNS-1338099 and by Rice University, the Extreme Science and Engineering Discovery Environment (XSEDE) by NSF under Grant No. DMR160057. Q.S. acknowledges the hospitality of the Aspen Center for Physics, which is supported by the NSF (Grant No. PHY-1607611), and the Institute for Materials Science at Los Alamos National Laboratory.

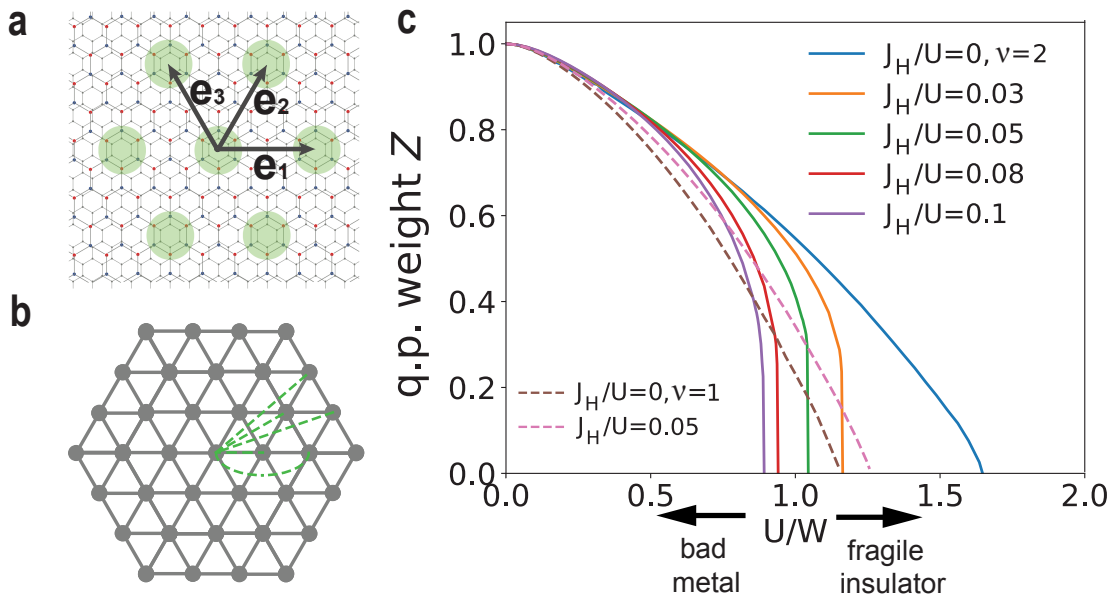

FIG. 1. **A graphene moiré system and the development of fragile insulator and bad metal. a,** Illustration of the morié superlattice, where $\mathbf{e_1}, \mathbf{e_2}, \mathbf{e_3}$ denote the superlattice basis vectors. The triangular lattice, marked by the green regions, results from a difference in the lattice constants between TGL and hBN. **b,** The bonds (dashed lines) for the hopping parameters, $t_1 - t_5$, of the effective tight binding model, which specify the hopping parameters for the other bonds in the moiré superlattice through the C_6 and M_y transformations (see Methods and Supplementary Information). **c,** The quasiparticle (q.p.) weight Z as a function of U/W. The results show the strong influence of the Hund's coupling J_H on the metal-insulator transition. For $J_H/U = 0, 0.03, 0.05, 0.08, 0.1$ at the half filling ($\nu = 2$) of the moiré bands, the Mott transition thresholds are $U_c/W = 1.65, 1.16, 1.04, 0.94, 0.89$, respectively. For $J_H/U = 0, 0.05$ at the quarter filling ($\nu = 1$), they are $U_c/W = 1.15, 1.26$, respectively.

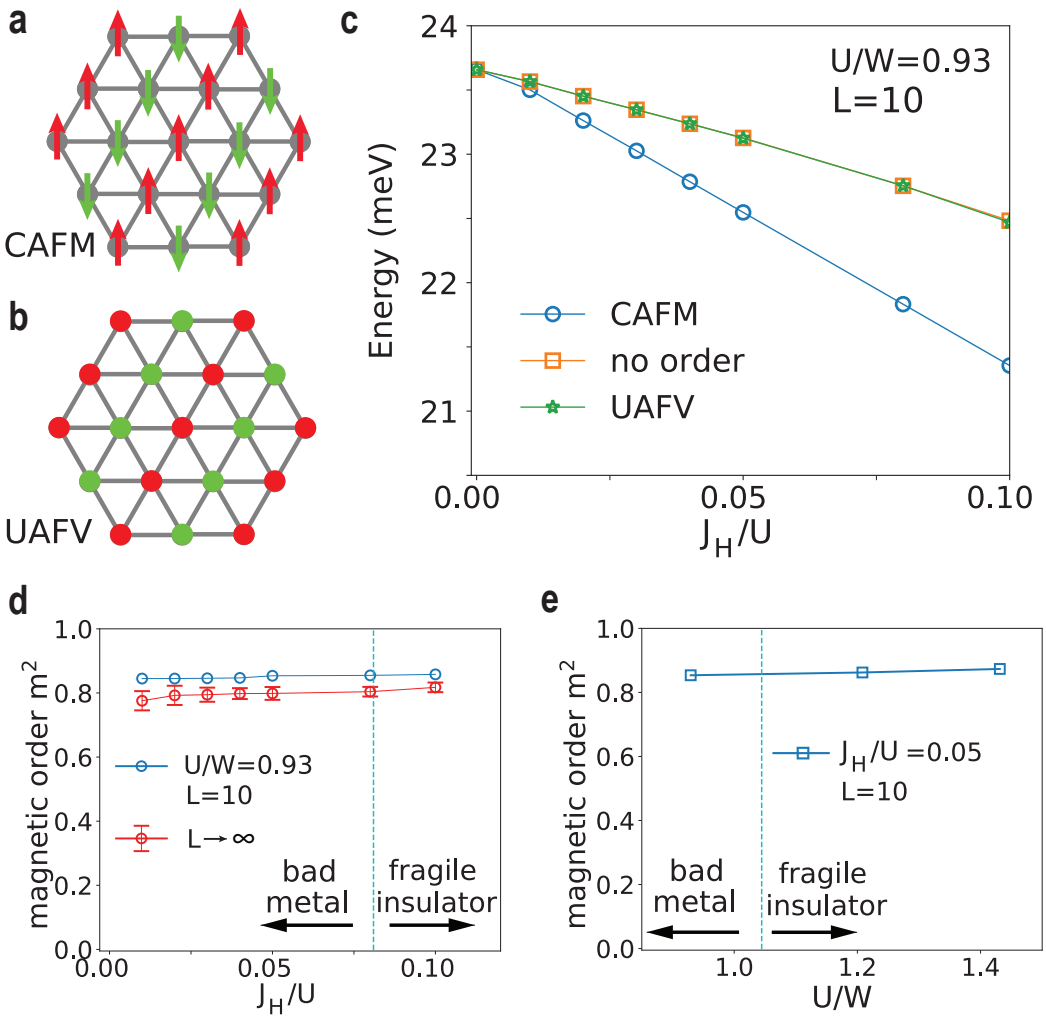

FIG. 2. **Ground state at half filling. a,** Illustration of the collinear antiferromagnetic order (CAFM). The red and green spins are opposite of each other. **b,** That of the uniaxial antiferrovalley order (UAFV). The red (green) sites represent $(n_+ - n_-) >(<) 0$. **c,** The ground state energy of the different states as a function of J_H/U for a fixed U/W. The VMC calculation is performed on a $L \times L$ geometry (Supplementary Information, Fig. S2). **d,** The magnetic order parameter (m^2) as a function of the Hund's coupling J_H/U for a fixed Hubbard interaction $U/W = 0.93$, at $L = 10$ and estimated from a finite size scaling ($L \to \infty$; see Supplementary Information, Fig. S4c,d). The magnetic order persists for J_H/U as small as 0.01. **e,** The magnetic order parameter (m^2) as a function of U/W for fixed $J_H/U = 0.05$.

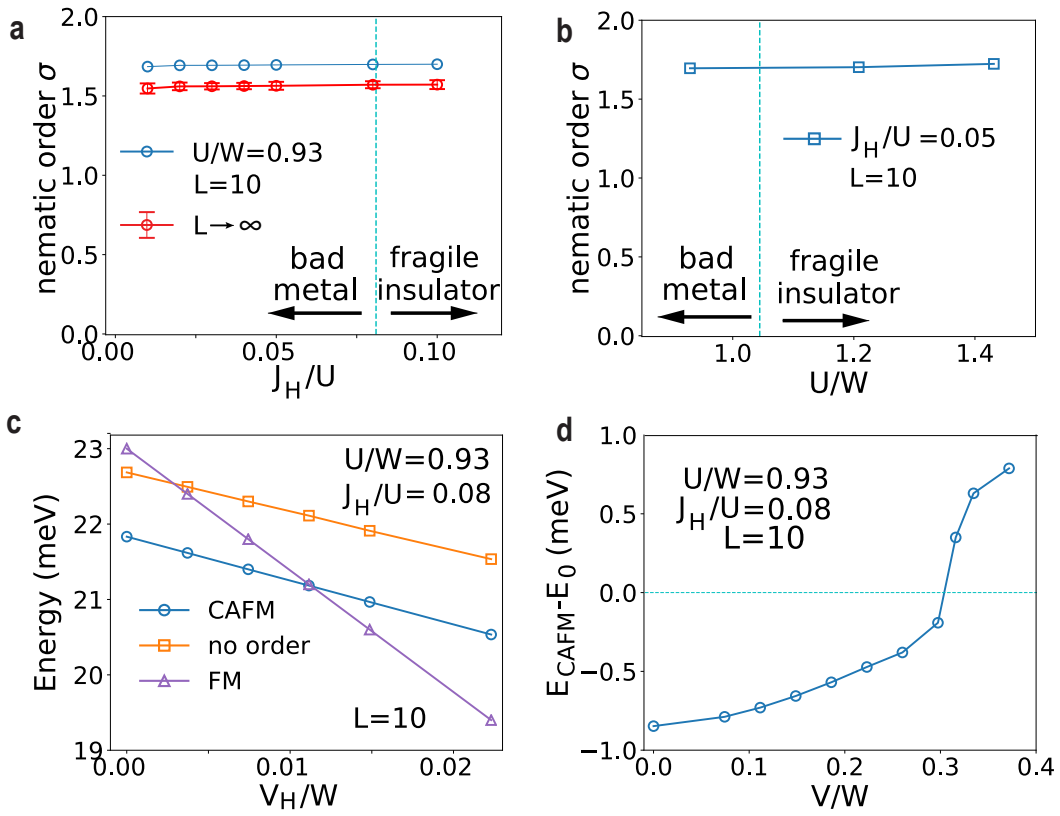

FIG. 3. **Nematic order and its stability. a,** The nematic order parameter (σ) as a function of the Hund's coupling J_H/U for fixed Hubbard interaction $U/W = 0.93$, calculated at $L = 10$ and estimated from a finite size scaling ($L \to \infty$, see Supplementary Information, Fig. S4c,d). **b,** The nematic order parameter (σ) as a function of U/W for fixed $J_H/U = 0.05$. **c,** The energy of the CAFM, non-ordered and ferromagnetic (FM) states *vs.* the nearest-neighbor exchange interaction V_H/W at $J_H/U = 0.08$ and $U/W = 0.93$. The threshold value for the FM state to have a lower energy is $V_H^1/W \approx 0.011$. **d,** The difference in the ground state energy between CAFM and the non-ordered state *vs.* the nearest-neighbor repulsion V/W at $J_H/U = 0.08$ and $U/W = 0.93$. The crossing interaction strength is $V^1/W \approx 0.31$.

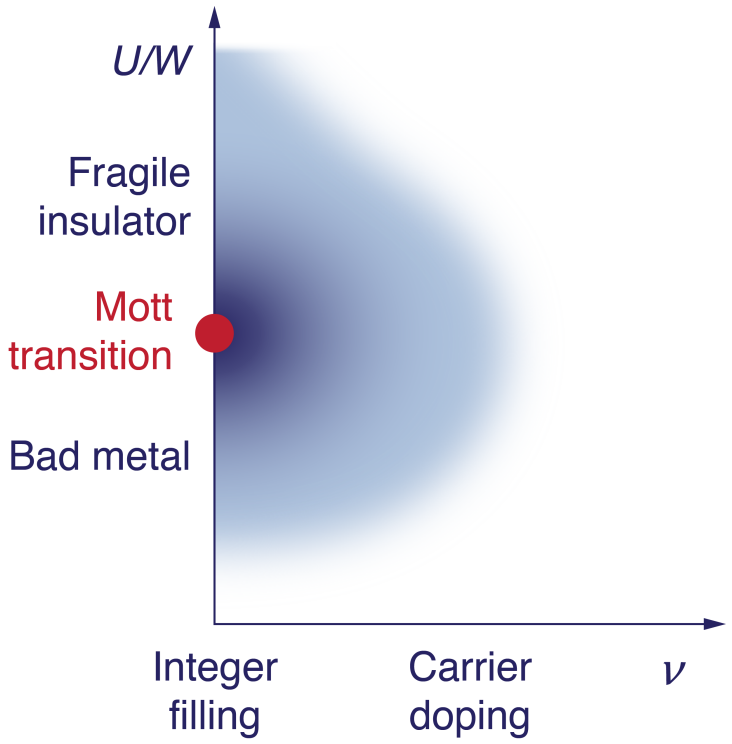

FIG. 4. **Schematic phase diagram involving fragile insulator and bad metal.** At an integer filling, the fragile insulator and bad metal are on the two sides of an electron localization transition (red point, a Mott transition) as a function of the interaction U/W. Both control the fluctuations in the magnetic and valley channels, thereby anchoring the physics in the regime where the carrier concentration (ν) is away from the integer filling (the shaded blue region).

Methods

The multiorbital Hubbard model The lowest energy levels of the original ABC stacked graphene (see Supplementary Information, Fig. S1) can be modeled as a two-band effective model with cubic band touching at K_+ and K_- momenta of the original BZ[35–37]. The perpendicular voltage bias generates an energy difference, Δ_V, between the top and bottom layers. The hBN layer provides a superlattice potential (Fig. 1a), with components at the reciprocal lattice vectors of the moiré lattice, which is the origin of the moiré bands. The combination of these terms lead to a two-orbital Hubbard model defined on a triangular lattice (*cf.* Fig. 1b), as given in Ref. 26:

$$\begin{aligned} H &= H_0 + H_U + H_V \,, \\ H_0 &= \sum_{\boldsymbol{k},\alpha\sigma} \epsilon_{\boldsymbol{k},\alpha} c^\dagger_{\boldsymbol{k},\alpha\sigma} c_{\boldsymbol{k},\alpha\sigma} \,, \\ H_U &= \sum_i \frac{U}{2} n_i^2 - J_H \sum_i \left(\frac{1}{4} n_{+,i} n_{-,i} + \boldsymbol{S}_{+,i} \boldsymbol{S}_{-,i} \right) \,, \\ H_V &= \sum_{\langle i,j \rangle} \left[V n_i n_j - \sum_{\alpha_1\alpha_2\sigma_1\sigma_2} V_H c^\dagger_{i,\alpha_1\sigma_1} c_{i,\alpha_2\sigma_2} c^\dagger_{j,\alpha_2\sigma_2} c_{j,\alpha_1\sigma_1} \right] \,. \end{aligned} \tag{1}$$

Here, $c^\dagger_{\boldsymbol{k},\alpha\sigma}$ creates an electron of wavevector $\boldsymbol{k}$, valley $\alpha = +$ or $-$ and spin σ, and H_0 describes the kinetic part, with hopping parameters up to the 5th nearest neighbors (*cf.* Fig. 1b) that specify the band dispersion $\epsilon_{\boldsymbol{k},\alpha}$. Additionally, H_U contains the onsite interactions: the Hubbard interaction U preserves the spin-valley U(4) symmetry, while the inter-valley Hund's coupling J_H breaks this symmetry down to U(1)$_c$×U(1)$_v$×SU(2)$_s$. The density and spin operators are defined as $n_{\alpha,i} = \sum_\sigma c^\dagger_{i,\alpha\sigma} c_{i,\alpha\sigma}$, $n_i = \sum_\alpha n_{\alpha,i}$, and $\boldsymbol{S}_{\alpha,i} = \frac{1}{2} \sum_{\sigma\sigma'} c^\dagger_{i,\alpha\sigma} \tau_{\sigma\sigma'} c_{i,\alpha\sigma'}$ respectively, with τ being the Pauli matrices. Finally, H_V contains the nearest-neighbor interactions: V is for density-density, and V_H for spin-valley exchange.

Variational Monte Carlo method We follow the VMC approach of Ref. 29, which incorporated a spin Jastrow factor in the Jastrow-Slater wavefunction[38] (in addition to the usual density Jastrow factor) to treat the correlation effect of the Hund's coupling non-perturbatively. The $L \times L$ geometry of our simulation is illustrated in the Supplementary Information, Fig. S2.

U(1) slave-spin method In the U(1) slave-spin method[30], the electron creation operator is expressed in terms of an xy spin operator $S^+_{i,\alpha\sigma}$, which represents the charge degree of freedom, and a fermionic 'spinon' operator $f_{i,\alpha\sigma}$: $c^\dagger_{i,\alpha\sigma} = S^+_{i,\alpha\sigma} f^\dagger_{i,\alpha\sigma}$. This is accompanied by a local constraint: $S^z_{i,\alpha\sigma} + 1/2 = f^\dagger_{i,\alpha\sigma} f_{i,\alpha\sigma}$. A set of self-consistent equations provide a saddle-point description,

which results in the quasiparticle weight $Z_{\alpha\sigma} = |\langle PS^{+}_{\alpha\sigma}P\rangle|^2$, where P is a projection operator that enforces the local constraint.

Magnetic order We calculate the spin structure factor defined as

$$S(\mathbf{Q}) = \frac{1}{N}\sum_{i,j}\langle \mathbf{S}_i \cdot \mathbf{S}_j\rangle\, e^{i\mathbf{Q}\cdot(\mathbf{R}_i-\mathbf{R}_j)}, \tag{2}$$

at $\mathbf{Q} = \mathbf{M}$, where N is the number of sites. The magnetic order parameter is $m^2 = S(\mathbf{M})/N$.

Nematic order The model, defined on the triangular lattice, has a C_6 rotational symmetry. However, weak terms that have been neglected in the Hamiltonian would reduce the symmetry to C_3. We have thus constructed the possible channels of nematic order from the irreducible representations of both the D_6 and D_3 point groups. The result is shown in Table I.

In TBG systems, the symmetry group is D_6 or D_3 depending on the twisting center, and the majority of the spectral weights stays on an effective triangular moiré superlattice. The same symmetry classification of the nematic orders applies to the TBG system.

Irr. Rep. (D_6)	Irr. Rep. (D_3)	Nematic order
B_1	A_1	$\frac{1}{\sqrt{6}}\sum_r (-1)^r B_r$
E_1	E	$\frac{1}{\sqrt{6}}\sum_r e^{i\frac{r\pi}{3}} B_r$, $\frac{1}{\sqrt{6}}\sum_r e^{i\frac{5r\pi}{3}} B_r$
E_2	E	$\frac{1}{\sqrt{6}}\sum_r e^{i\frac{2r\pi}{3}} B_r$, $\frac{1}{\sqrt{6}}\sum_r e^{i\frac{4r\pi}{3}} B_r$

TABLE I. **The classification of the nematic order.** Here, the nearest-neighbor-bond variables are $B_r = \frac{1}{N}\sum_i \langle \mathbf{S}_i \cdot \mathbf{S}_{i+e_r}\rangle$, where $\{e_r\}_{r=1,..,6}$ denote the set of six nearest neighbors, with e_1, e_2, e_3 shown in Fig. 1a, and $e_4, e_5, e_6 = -e_1, -e_2, -e_3$.

The nematic order that is important for the present work is in the E_2/E channel, in the two classification schemes respectively:

$$\sigma = \frac{1}{N}\sum_i \left[\langle \mathbf{S}_i \cdot \mathbf{S}_{i+e_1}\rangle + e^{i\frac{2\pi}{3}}\langle \mathbf{S}_i \cdot \mathbf{S}_{i+e_2}\rangle + e^{i\frac{4\pi}{3}}\langle \mathbf{S}_i \cdot \mathbf{S}_{i+e_3}\rangle\right] . \tag{3}$$

Data availability The data that support the findings of this study are available from the corresponding author upon reasonable request.

Supplementary Information

Bandstructure and Fermi surface

We outline the bandstructure, both over an extended energy range and for the bands retained in the model, and the Fermi surface[14,26,39]. We will use the notation of Ref. 26 for the most part. If one firstly ignores the hBN layer and focuses on the ABC stacked trilayer graphene (*cf.* Fig. S1), the bare hopping parameters are known in the literature[40], and there is an energy difference Δ_V between the top and bottom layers. There is a cubic band touching at each of the two momenta, K_{lbz} and K'_{lbz} of the original (large) BZ, which are labeled as valley $+$ and $-$. One can integrate out the higher energy states to construct an effective Hamiltonian for the electron states associated with the top (t) and bottom (b) layers. The low energy behavior in each valley is described by a two band model, counting the contributions from the A sublattice of the top layer and B sublattice from the bottom layer[35]. The other degrees of freedom are gapped out because of the large direct interlayer hybridization: *cf.* the tight-binding parameters, as illustrated in Fig. S1, are $\gamma_0 \approx -3$ eV, $\gamma_1 \approx 380$ meV, $\gamma_3 \approx 293$ meV, $\gamma_4 \approx 144$ meV (Ref. 40). The aligned hBN substrate creates a potential for the adjacent graphene layer. This potential comprises components at the morié superlattice Bravais vectors for each of the two valleys. Diagonalizing this Hamiltonian numerically up to the 5th $q_M = \frac{4\pi}{3a_M}$, where $a_M \approx \frac{a_1 a_2}{a1-a2} \approx 58a$ with $a_{1,2}$ being the lattice constants of the TLG and hBN, yields the band dispersion in the extended energy range (Fig. S3b,c). The two sets of moiré bands are separated by a gap, as opposed to be gapless with Dirac points in the TBG case.

For different signs of Δ_V, the Fermi energy crosses two different sets of the moiré bands: Those for $\Delta_V > 0$ have nonzero Chern numbers, while those for $\Delta_V < 0$ do not. In the latter case, the effective Hamiltonian is a two-band Hubbard model defined on the triangular lattice illustrated in Fig. 1a, as presented in Eq. (1) (Ref. 26). The kinetic part has the following form:

$$H_0 = -\sum_{ij} t_{ij} c^\dagger_{+\sigma} c_{+\sigma} - \sum_{ij} t^*_{ij} c^\dagger_{-\sigma} c_{-\sigma} + h.c., \tag{S1}$$

where $\pm$ is the valley index and $\sigma =\uparrow,\downarrow$ is the spin index. The time reversal symmetry dictates $\epsilon_{\boldsymbol{k},+} = \epsilon_{-\boldsymbol{k},-}$. The complex hopping terms break the spin-valley U(4) symmetry down to $\mathrm{U}(2)_+ \times \mathrm{U}(2)_-$ (Refs. 26,39). The tight-binding parameters, as illustrated in Fig. 1b of the main text; for the case of $\Delta_V = -20$ meV are $t_1 = 1.583e^{i0.169\pi}$ meV, $t_2 = -1.108$ meV, $t_3 = 0.732e^{-i0.653\pi}$ meV and $t_4 = t_5^* = 0.323e^{-i0.069\pi}$ meV (Ref. 26). Those for the other symmetry-related bonds are generated by the C_6 rotation and M_y reflection. This morié band

structure is shown in Fig. S3a, with a bandwidth $W = 26.9$ meV. The path within the moiré BZ, along which the band structure is shown, can be found in Fig. S3d. The corresponding Fermi surfaces at half filling are presented in Fig. S3d,e,f.

Details of the Variational Monte Carlo method

The VMC approach is adapted from that of Ref. 29, which considered a square lattice. In the present study, our model is defined on a triangular lattice. As in Ref. 29, a spin Jastrow factor is used, in addition to the usual density Jastrow factor, to treat the correlation effect of the Hund's coupling. The uncorrelated state $|\Phi_0\rangle$ is specified by the following auxiliary (quadratic) Hamiltonian[41,42]:

$$\begin{aligned}\mathcal{H}_{\text{aux}} = &-\sum_{ij,\alpha\sigma}(1+\delta\tilde{\alpha}_{ij})t_{ij}\left(c^{\dagger}_{i,\alpha\sigma}c_{j,\alpha\sigma}+h.c.\right)-\sum_{ij,\sigma}\delta\tilde{t}_{ij}\left(c^{\dagger}_{i,+\sigma}c_{j,-\sigma}+h.c.\right)\\ &+\sum_{i,\alpha\sigma}\tilde{\mu}_{\alpha}c^{\dagger}_{i,\alpha\sigma}c_{i,\alpha\sigma}+\Delta^{AFM}_{\alpha}\left(\sum_{i,\alpha}e^{i\mathbf{Q}_{mag}\cdot\mathbf{R}_i}c^{\dagger}_{i,\alpha\uparrow}c_{i,\alpha\downarrow}+h.c.\right)\\ &+\sum_{i,\alpha\sigma}\alpha\Delta^{AFV}\left(e^{i\mathbf{Q}_{v}\cdot\mathbf{R}_i}c^{\dagger}_{i,\alpha\sigma}c_{i,\alpha\sigma}+h.c.\right)\end{aligned} \tag{S2}$$

where $\delta\tilde{\alpha}_{ij}$, $\delta\tilde{t}_{ij}$, $\tilde{\mu}_{\alpha}$, and Δ^{AFM}_{α}, Δ^{AFV} are variational parameters and real. The first two terms came from the renormalization of the hopping. For the intra-valley hopping, we fix the phase to be the same as for the non-interacting limit, while introducing the amplitude scaling variables $(1+\delta\tilde{\alpha}_{ij})$. The presence of $\Delta^{AFM}_{\alpha}(\Delta^{AFV}) \neq 0$, implies magnetic (valley) order. By choosing $\mathbf{Q}_{mag}$ ($\mathbf{Q}_v$) to be $\mathbf{K}$ $(\frac{4}{3}\pi, 0)$ or $\mathbf{M}$ $(\pi, \frac{1}{\sqrt{3}}\pi)$, we can have either three sublattice (120°)-like or two sublattice magnetic (valley) orders. The geometry is shown in S2, with the periodic boundary condition (PBC) for both directions. Each direction has a linear dimension L; the total number of sites is $N = L \times L$. For each L, all the results for the order parameters, from Fig. 2 through Fig. S4a,b, are determined by measuring in the interior $(L-1)\times(L-1)$ region. The results are not sensitive to the boundary condition. We have also done measurements for the central $(L-2)\times(L-2)$ region and the central 4×4 region, and the results are similar to those from the $(L-1)\times(L-1)$ measurement. This is illustrated by comparing Fig. S4c,d and Fig. S4e,f.

Finite size scaling for the order parameters

The magnetic and nematic orders with $L = 8, 10, 12, 14, 16$ are shown in Fig. S4a,b. To extrapolate to the thermodynamical limit, a finite size scaling over the system size is performed and is illustrated in Fig. S4c,d. when the measurements were done from the interior $(L-1)\times(L-1)$ region for each L. (Fig. S4e,f, show the results for comparison, when the measurements are done

in the central 4×4 region for every L.) Polynomial fittings, with the exponent up to 2, are performed. The error bars are estimated as the standard deviation between the simulated results and the estimated values of the fitted curves.

Hartree-Fock calculation

We perform Hartree-Fock calculations to study the phase diagram and stability of the CAFM phase in the presence of the nearest-neighbor interaction terms of H_V. Here, except for the FM, CAFM, UAFV and paramagnetic phases that have been studied by the VMC method, we also include the charge-ordered phase with wavevector $\mathbf{K}$ (CO-K), which is a three-sublattice order with the particle numbers being different in the different sublattices. This type of order can be favored when the nearest-neighbor repulsion V is sufficiently large. Finally, with a sizable $t_2^2/|t_1|^2 \approx 0.49$, we can expect that the CAFM phase is energetically favored compared with any three-sublattice AFM. Our calculation of the AFM-K phase indicates that this is indeed the case.

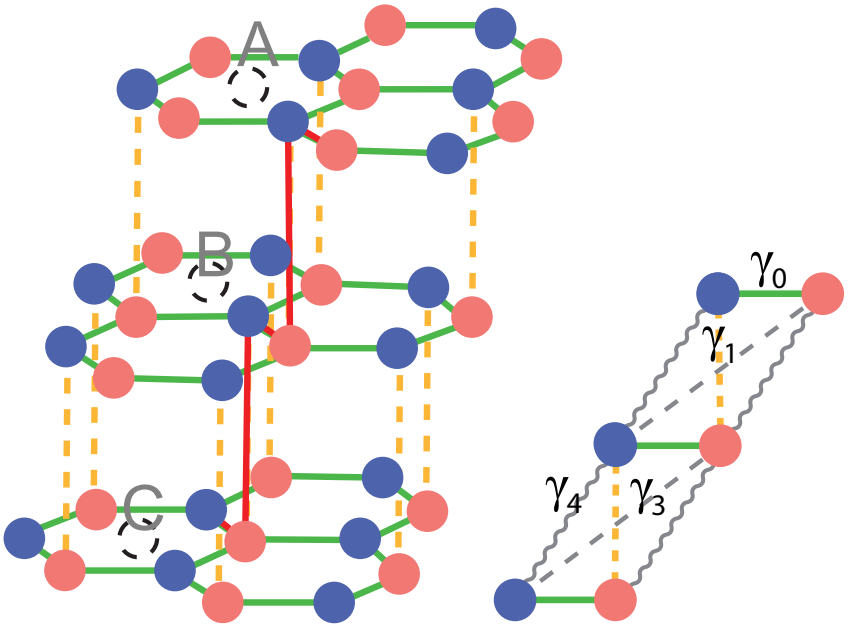

FIG. S1. **Illustration of the ABC stacked trilayer graphene.** The γ's label the tight-binding parameters that are used to construct the TLG bandstructure[40].

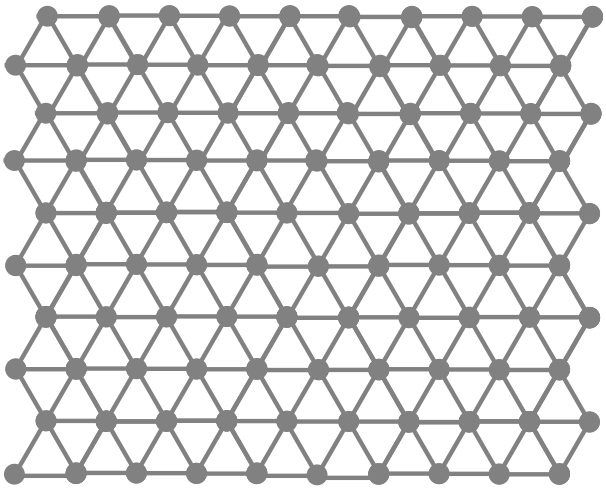

FIG. S2. **The real space structure of the morié superlattice for the VMC calculation.** Illustrated here is the $L \times L$ case with $L = 10$. The periodic boundary condition is implemented for each direction.

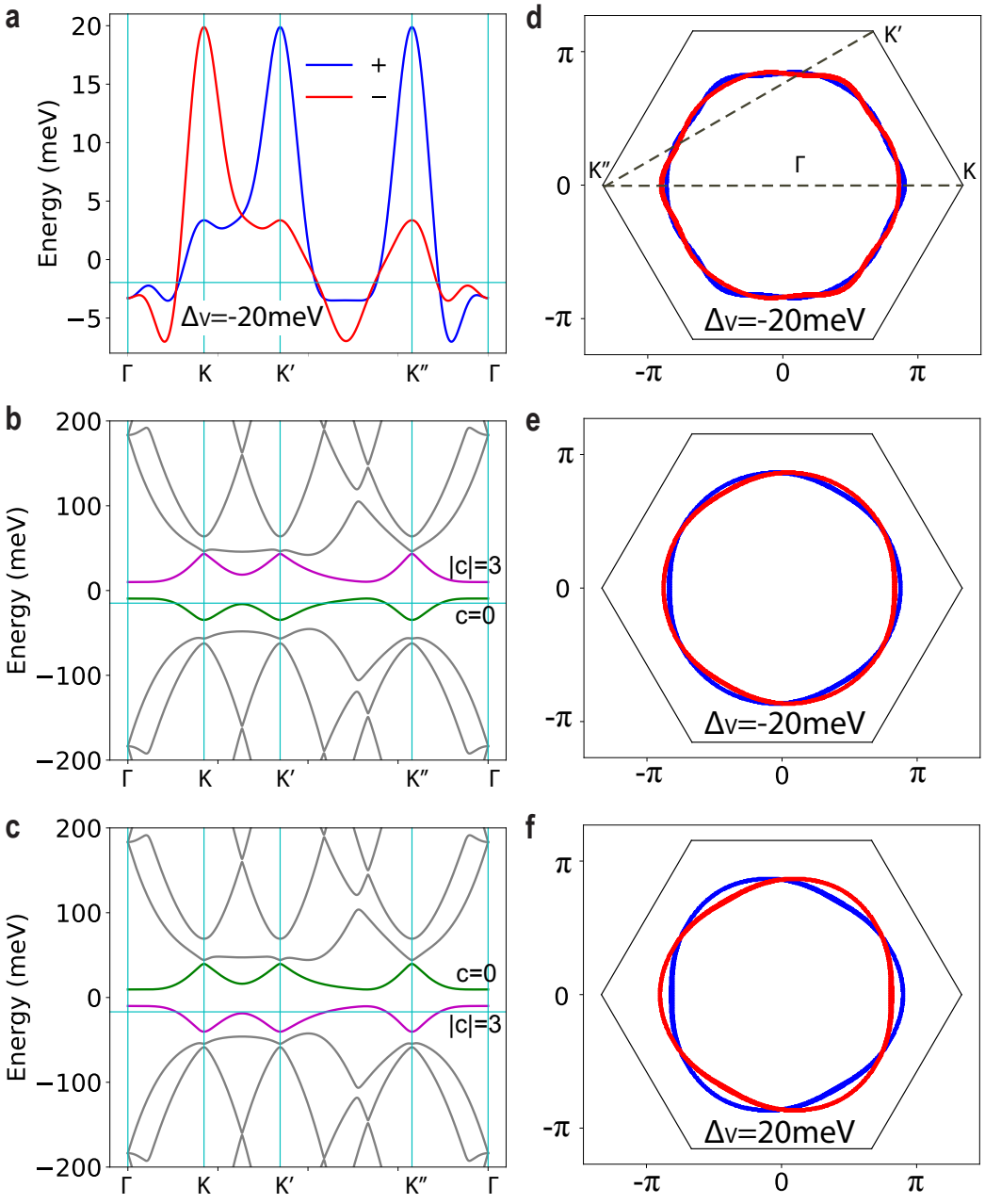

FIG. S3. **Bandstructure and Fermi surface. a,** The band structure of the two-orbital tight-binding model, with the perpendicular bias energy $\Delta_V = -20$ meV, for both valleys. The horizontal cyanic line represents the Fermi energy for half filling. **b**, The band structure of the continuum model for the $+$ valley, with $\Delta_V = -20$ meV. The Fermi energy crosses the band with the Chern number $c = 0$. **c,** The counterpart of **b** for $\Delta_V = 20$ meV. The Fermi energy crosses the band with nonzero c. **d, e, f,** The Fermi surface at half filling for the tight binding model, and for the continuum models with $\Delta_V = -20$ meV and $\Delta_V = 20$ meV.

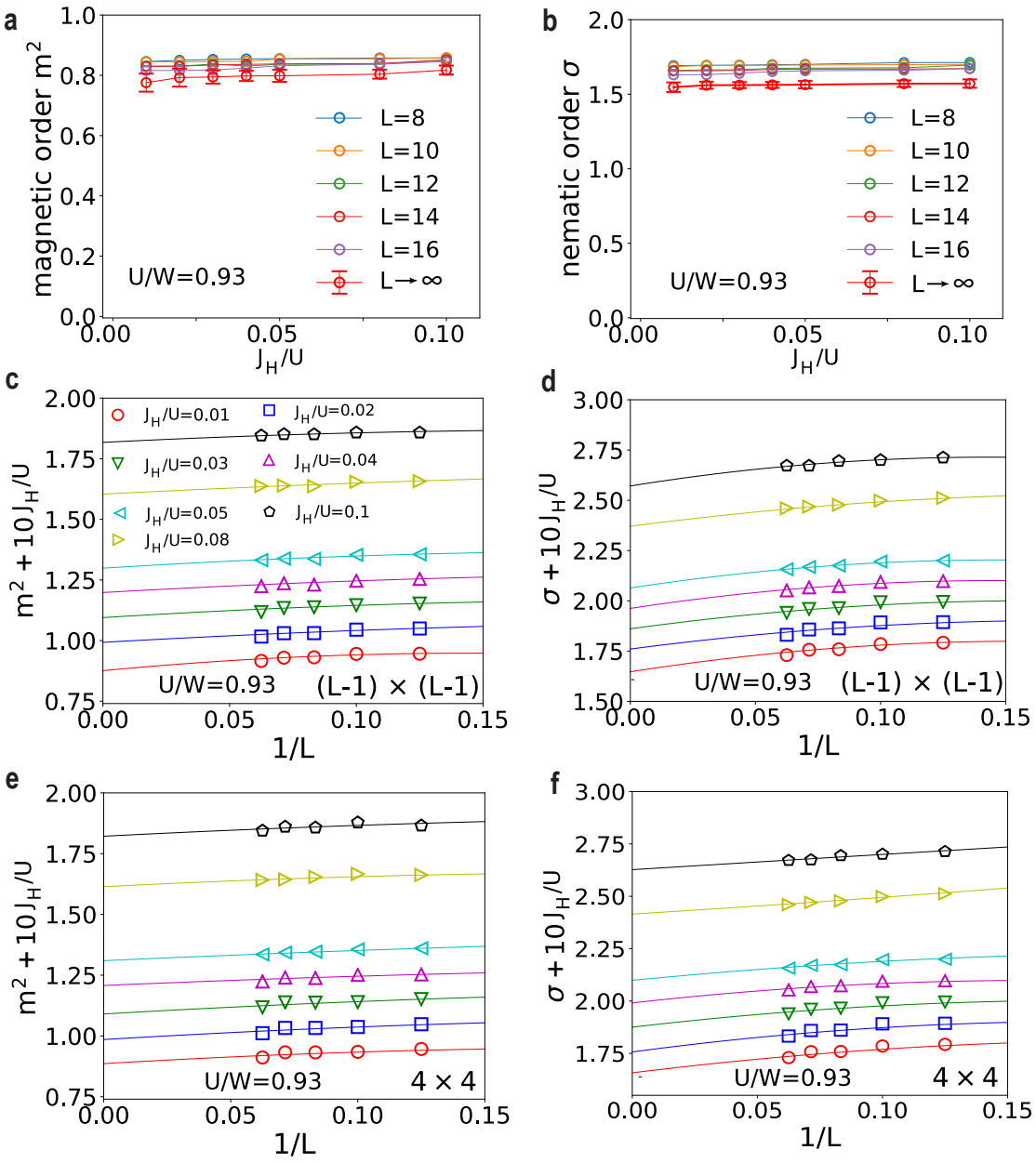

FIG. S4. **Size dependence and finite size scaling of the order parameters.** **a,** Magnetic order parameter m^2 as a function of J_H/U for a fixed U/W, at different sizes $L = 8, 10, 12, 14, 16$ and in the limit $L \to \infty$ based on finite size scaling. **b,** The counterpart of **a** for the nematic order parameter σ. **c, d,** Finite size scaling of the magnetic and nematic order parameters, measured in the interior $(L-1) \times (L-1)$ region, for the different values of J_H/U at a fixed U/W. The different J_H/U cases are shifted by "$10J_H/U$" for clarity. **e, f,** The counterparts of **c** and **d** with the order parameters measured in the central 4×4 region.

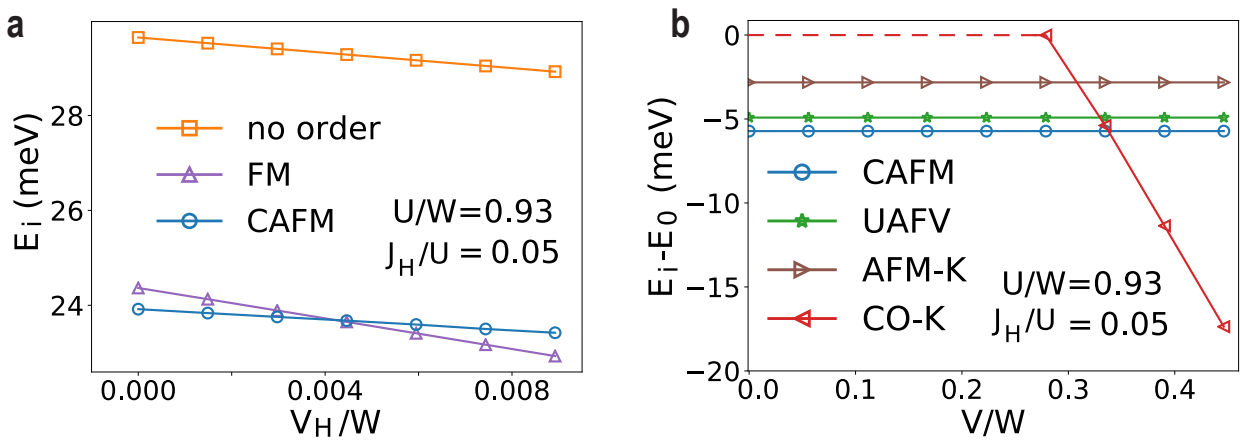

FIG. S5. **Result of the self-consistent Hartree-Fock calculation. a**, The ground state energies of the various symmetry-broken phases and the paramagnetic phase versus the nearest-neighbor exchange interaction V_H/W with fixed $U/W = 0.93$ and $J_H/U = 0.05$. Here i includes no order, ferromagnetic (FM) and collinear antiferromagnetic order (CAFM). **b,** The difference between the ground state energy of a broken symmetry phase i and that of the paramagnetic phase 0 versus the nearest-neighbor density-density interaction V/W. Here, i includes CAFM, the uniaxial antiferrovalley (UAFV) order, collinear antiferromagnetic order with wavevector $\mathbf{K}$ (AFM-K) and charge order with wavevector $\mathbf{K}$ (CO-K, which has no solution in the parameter region corresponding to the dashed portion of the line).